A fast and robust computational method for the ionization cross sections of the driven Schrödinger equation using an $\mathcal{O}(N)$ multigrid-based scheme

S. Cools[a], W. Vanroose[a]

[a]*Applied Mathematics Research Group, Department of Mathematics and Computer Science, University of Antwerp, Middelheimlaan 1, 2020 Antwerp, Belgium*

arXiv:1412.1953v4 [physics.comp-ph] 17 Sep 2015

Abstract

This paper improves the convergence and robustness of a multigrid-based solver for the cross sections of the driven Schrödinger equation. Adding an Coupled Channel Correction Step (CCCS) after each multigrid (MG) V-cycle efficiently removes the errors that remain after the V-cycle sweep. The combined iterative solution scheme (MG-CCCS) is shown to feature significantly improved convergence rates over the classical MG method at energies where bound states dominate the solution, resulting in a fast and scalable solution method for the complex-valued Schrödinger break-up problem for any energy regime. The proposed solver displays optimal scaling; a solution is found in a time that is linear in the number of unknowns. The method is validated on a 2D Temkin-Poet model problem, and convergence results both as a solver and preconditioner are provided to support the $\mathcal{O}(N)$ scalability of the method. This paper extends the applicability of the complex contour approach for far field map computation [*S. Cools, B. Reps, W. Vanroose, An Efficient Multigrid Calculation of the Far Field Map for Helmholtz and Schrödinger Equations, SIAM J. Sci. Comp. 36(3) B367–B395, 2014*].

1. Introduction

Over the past decades significant work has been performed on the computational simulation of breakup problems in atomic and molecular physics. The cross sections of electron-impact ionization problems were calculated for atoms and molecules in [24, 28, 2, 23, 34]. However, the classical algorithms for the computation of the ionization cross sections for a general Schrödinger type scattering problem are notably very demanding in terms of computational resources, and hence require supercomputing infrastructure. This computational cost primarily originates from the computation of the high-dimensional scattering solutions governed by Schrödinger's equation, which are notoriously hard to obtain using either classical direct methods or iterative solvers. Hence, numerical simulations of the far field behaviour for molecular break-up problems are generally computationally challenging. The aim of this work is to design an efficient and scalable method for the computation of the cross sections of the d-dimensional driven Schrödinger equation. Moreover, we aim at computing the single differential cross section (SDCS) and total cross section (TCS) for Schrödinger type scattering problems using a multigrid-based method that scales linearly in the number of unknowns.

Multigrid [6] is an efficient iterative solution method for the large and sparse linear systems that appear in the numerical solution of Laplace-type partial differential equations (PDEs). The method relies upon a hierarchy of discretizations of the problem to accelerate convergence to the solution at the finest discretization level. The key concept of the multigrid method is the synergy between the *smoother*, i.e. a basic iterative update step such as weighted Jacobi or Gauss-Seidel that is applied at each level, and a coarse grid correction scheme that solves the error equation on a coarser discretization level. Consequently, the interpolated error

Email addresses: siegfried.cools@uantwerpen.be (S. Cools), wim.vanroose@uantwerpen.be (W. Vanroose)

is used to correct the fine-level guess to the solution [6, 7]. From a spectral analysis point of view, the smoother removes the oscillatory parts from the error, resulting in a remaining error that is smooth enough to be represented at the coarser levels of the discretization hierarchy. Applying this recursively leads to an $\mathcal{O}(N)$ scheme for the solution of Laplace-type PDEs, where N is the number of unknowns at the finest level. The multigrid method is therefore commonly used to solve high-dimensional Poisson problems, where it is particularly efficient due to its scalability. Additionally, multigrid is in practice often used as a preconditioner to accelerate the convergence of Krylov subspace iterations such as Conjugate Gradients (CG) or GMRES [33]. Multigrid-preconditioned Krylov methods have been successfully applied as solvers for e.g. fluid flow models, see [12]. Moreover, it has been shown in the literature that the use of multigrid as a Krylov method preconditioner results in an efficient and scalable solution method for Laplace-type problems, featuring a convergence rate which is independent of the number of unknowns [32].

Although multigrid is customarily applied as both a solver and preconditioner for a wide range of Laplace-type PDEs, it is well-known that the classical multigrid method (like any iterative solver) utterly breaks down when applied to Helmholtz or Schrödinger problems. The reason for this convergence failure is best understood by analyzing the spectral properties of the corresponding operator. Due to the intrinsic indefiniteness of the discretized Helmholtz operator, the occurrence of near-zero coarse level eigenvalues destroys the stability of both smoother and two-grid correction scheme, leading to a possibly highly instable multigrid scheme [13, 15]. In the past decades many efforts have been performed to overcome these stability issues of multigrid for Helmholtz equations. It has been proposed in [14] and [21] that multigrid and ILU can be successfully used as a solver for the complex shifted (i.e. damped) Helmholtz equation. This perturbed problem is known as *complex shifted Laplacian* (CSL), and is commonly used as a preconditioner for Helmholtz problems [5]. Alternatively, the underlying numerical grid can be rotated into the complex domain to yield an equivalent damped Helmholtz problem, which is known as *complex stretched grid* (CSG) [27]. This technique shows significant resemblances to *Exterior Complex Scaling* (ECS) [31].

In this paper the properties of the multigrid method on damped Helmholtz and Schrödinger equations are exploited to construct an efficient computational method for the far field map (ionization cross sections) of Helmholtz (Schrödinger) type scattering problems. The computation of the far field map can typically be seen as a two-step process. The first step consists of solving the underlying Helmholtz or driven Schrödinger equation on a bounded numerical domain with absorbing boundary conditions, whereas in the second step an integral over the scattering solution on this domain has to be calculated [20, 9]. The main computational bottleneck is generally the first step, since this requires the solution of a large scale scattering problem that is typically hard to obtain using classical iterative methods. However, in [10] it was proposed that the classical far field integral over the real-valued d-dimensional bounded domain can alternatively be replaced by an integral over a complex-valued manifold. Furthermore, the proposed technique was validated [10] by showing that the complex contour approach yields an identical far field map. Moreover, after the deformation of the integral, the first step in the calculation now consists of solving a damped Helmholtz or Schrödinger equation, which can be very efficiently achieved using e.g. multigrid methods. The main computational bottleneck in the far field map computation is hence overcome, since the numerical solution on the complex domain can effectively be obtained using a scalable iterative method. However, it was reported in [10] that the proposed method fails for a range of negative energies where single ionization is present.

In this work we extend the complex contour approach introduced in [10] to compute the ionization cross sections of 2D Schrödinger type scattering problems, such that it works for all energies, including those energy regimes where single ionization waves dominate the solution. The multigrid method used for the solution of the complex-valued driven Schrödinger problem (step 1) is extended by the addition of a so-called *Coupled Channel Correction Scheme* (CCCS) [18, 22], which ensures the efficiency of the proposed solver for all possible energy levels by specifically eliminating the bound states, i.e. low-dimensional localized waves travelling along the domain edges. The Coupled Channel Correction Scheme is derived analytically, and we

expound on its numerical properties through an eigenvalue analysis. Numerical results in 2D are provided to illustrate that the combination of multigrid and the Coupled Channel Correction Scheme (MG-CCCS) effectively leads to a fast, scalable and robust iterative scheme for solving the driven Schrödinger equation for any energy regime.

The outline of the article is as follows. Section 2 introduces the general notations and basic concepts used throughout this work. In Section 3 we briefly revisit the complex contour method for the computation of the far field map, which was initially proposed in [10], and we comment on the spectral properties of the complex rotated Schrödinger equation. This discussion motivates the need for the so-called Coupled Channel Correction Scheme (CCCS) introduced in Section 4, which is used to compensate for the deterioration of multigrid convergence in certain energy regimes where bound states dominate the solution. Section 5 expounds on the implementation of the Coupled Channel scheme and the influence of the complex rotation angle on numerical accuracy. Taking into account these remarks, the single differential and total cross sections of a 2D Temkin-Poet model problem are computed using the MG-CCCS method. We illustrate the efficiency of the combined MG-CCCS method both as a solver and a preconditioner in Section 6. Furthermore, the robustness of the MG-CCCS preconditioned Krylov solvers with respect to the energy of the system is demonstrated in this section. Section 7 concludes this work alongside a discussion on the topic.

2. The Schrödinger equation and the far field map

The driven time-independent Schrödinger equation describing a system consisting of one positively charged nucleus located at the origin and two negatively charged electrons with spatial coordinates $\mathbf{r}_1$ and $\mathbf{r}_2 \in \mathbb{R}^3$ is given by

$$(\mathcal{H} - E)\,\psi(\mathbf{r}_1, \mathbf{r}_2) = \xi(\mathbf{r}_1, \mathbf{r}_2). \tag{1}$$

The operator $\mathcal{H}$ denotes the Hamiltonian

$$\mathcal{H} = -\frac{1}{2m}\triangle_{\mathbf{r}_1} - \frac{1}{2m}\triangle_{\mathbf{r}_2} + V_1(\mathbf{r}_1) + V_2(\mathbf{r}_2) + V_{12}(\mathbf{r}_1, \mathbf{r}_2),$$

where the mass $m > 0$ scales the Laplacians. The right hand side $\xi(\mathbf{r}_1, \mathbf{r}_2)$ in (1) can model either an incoming electron that impacts the system [28], or alternately, represents the dipole operator working on a ground state if the model is used to compute photoionization [35]. For these break-up problems the solution $\psi(\mathbf{r}_1, \mathbf{r}_2)$ is an outgoing wave in any direction and leads to a six-dimensional problem on an unbounded domain. Note that in the context of simulating electron impact ionization the two electrons, namely the electron particle in the target and the impinging electron, are indistinguishable and need to be described on equal footing. This naturally leads to the 6D Schrödinger equation (1). The potential is typically split into a sum of one-body potentials V_1 and V_2, and a two-body potential V_{12}. Here the one-body potentials model the attraction of each electron by the nuclear charge, whereas the two-body potential simulates the electron-electron repulsion. More generally, for a system containing d particles, the potential $V(\mathbf{r}_1, \ldots, \mathbf{r}_d)$ can be written as

$$V(\mathbf{r}_1, \ldots, \mathbf{r}_d) = \sum_{i=1}^{d} V_i(\mathbf{r}_i) + \sum_{i<j}^{d} V_{ij}(\mathbf{r}_i, \mathbf{r}_j) = \bar{V}_1(\mathbf{r}_1, \ldots, \mathbf{r}_d) + \bar{V}_2(\mathbf{r}_1, \ldots, \mathbf{r}_d). \tag{2}$$

We use $\bar{V}_1$ to denote the sum of all one body potentials and $\bar{V}_2$ for the sum of the two-body potentials throughout the following sections.

2.1. The partial wave expansion

At large distances from the object, the solution of (1) behaves like a spherical wave emerging from the center of mass of the system. Equation (1) is therefore commonly rewritten in spherical coordinates [2, 34], where

the Laplacian operator splits into a radial operator and an angular differential operator [1]. The coordinates are written as $\mathbf{r}_1 = (\rho_1, \Omega_1)$ and $\mathbf{r}_2 = (\rho_2, \Omega_2)$, where Ω_i denotes the solid angle in the three-dimensional space. The solution is represented by the series

$$\psi(\mathbf{r}_1, \mathbf{r}_2) = \sum_{l_1=0}^{\infty} \sum_{m_1=-l_1}^{l_1} \sum_{l_2=0}^{\infty} \sum_{m_2=-l_2}^{l_2} \psi_{l_1 m_1, l_2 m_2}(\rho_1, \rho_2) Y_{l_1 m_1}(\Omega_1) Y_{l_2 m_2}(\Omega_2), \tag{3}$$

where $Y_{l_i m_i}(\Omega_i)$ are the spherical harmonics, i.e. the eigenfunctions of the angular differential operator of the Laplacian in spherical coordinates [1]. The above decomposition is commonly referred to as the partial wave expansion. After substitution of (3) into the Schrödinger equation (1) and an integration over Ω_1 and Ω_2 one obtains an equation for the radial components $\psi_{l_1\, m_1, l_2\, m_2}(\rho_1, \rho_2)$ for all $l_1 \geq 0, l_2 \geq 0, |m_1| \leq l_1, |m_2| \leq l_2$, that is coupled to all other partial waves, i.e.

$$\begin{aligned} &\left[-\frac{1}{2m} \triangle_{l_1, l_2} - E\right] \psi_{l_1 m_1, l_2 m_2}(\rho_1, \rho_2) \\ &+ \sum_{l_1'=0}^{\infty} \sum_{m_1'=-l_1'}^{l_1'} \sum_{l_2'=0}^{\infty} \sum_{m_2'=-l_2'}^{l_2'} V_{l_1\, m_1\, l_2\, m_2; l_1'\, m_1', l_2'\, m_2'}(\rho_1, \rho_2)\ \psi_{l_1' m_1', l_2' m_2'}(\rho_1, \rho_2) = \xi_{l_1 m_1, l_2 m_2}. \end{aligned} \tag{4}$$

Note that the system decouples when the potentials V_1, V_2 and V_{12} are spherically symmetric. The differential operators only appear on the diagonal blocks of the resulting coupled system. These diagonal blocks take the form of a 2-dimensional driven Schrödinger equation

$$\left(-\frac{1}{2}\Delta + V(\mathbf{x}) - E\right) u(\mathbf{x}) = f(\mathbf{x}), \quad \text{for } \mathbf{x} = (x, y) \in \mathbb{R}^2, \tag{5}$$

for a system with unit mass, where Δ is the 2-dimensional Laplacian, $V(\mathbf{x})$ is a scalar potential, E is the total energy of the system, u is the outgoing partial wave function and f is the right-hand side, representing the effect of an incoming wave (electron scattering) or the influence of an optical perturbation such as interaction with light (photoionization). The operator $H = -\frac{1}{2}\Delta + V(\mathbf{x})$ is the Hamiltonian. The potential $V(\mathbf{x})$ includes angular potentials like $l_i(l_i+1)/x^2$ $(i = 1, 2)$, related to the partial wave angular momentum. Note that the above formulation directly extends to the case where three or more particles are considered. Equation (5) then generalizes to

$$\left(-\frac{1}{2}\Delta^d + V(\mathbf{x}) - E\right) u(\mathbf{x}) = f(\mathbf{x}), \quad \text{for } \mathbf{x} \in \mathbb{R}^d, \tag{6}$$

where $d = 2, 3, \ldots$ corresponds to the number of electrons in the system, and hence the dimension of the radial partial wave equation. The operator Δ^d is the related d-dimensional partial wave Laplacian.

2.2. The 2D Schrödinger equation: notation and basic properties

As suggested above, for the 6D scattering problem (1) the diagonal blocks of the coupled system (4) take the form of a two-dimensional Schrödinger equation

$$\left(-\frac{1}{2}\Delta + V_1(x) + V_2(y) + V_{12}(x, y) - E\right) u(x, y) = f(x, y), \quad x, y \geq 0, \tag{7}$$

with boundary conditions

$$\begin{cases} u(x, y) = 0 & \text{for} \quad x = 0 \quad \text{or} \quad y = 0, \\ \text{outgoing} & \text{for} \quad x \to \infty \quad \text{or} \quad y \to \infty, \end{cases}$$

where $V_1(x)$ and $V_2(y)$ are the one-body potentials and $V_{12}(x, y)$ is a two-body potential. Since the arguments x and y are in fact radial coordinates in the partial wave expansion, homogeneous Dirichlet boundary conditions are imposed at the $x = 0$ and $y = 0$ boundaries. The potentials V_1, V_2 and V_{12} are generally analytical functions that decay as the radial coordinates x and y become large.

2.3. Relation to the Helmholtz equation

Depending on the total energy of the system $E \in \mathbb{R}$, the above Schrödinger system allows for scattering solutions, in which case equation (6) can be reformulated as a d-dimensional Helmholtz equation of the form

$$\left(-\Delta - k^2(\mathbf{x})\right)\, u(\mathbf{x}) = g(\mathbf{x}), \quad \text{for } \mathbf{x} \in \mathbb{R}^d, \tag{8}$$

where the spatially dependent wavenumber $k(\mathbf{x})$ is defined by $k^2(\mathbf{x}) := 2(E - V(\mathbf{x}))$ and the right-hand side is $g(\mathbf{x}) = 2f(\mathbf{x})$. The experimental observations from this type of quantum mechanical systems are typically far field maps of the solution [34]. In many quantum mechanical systems the potential $V(\mathbf{x})$ is an analytical function, which suggests analyticity of the spatially dependent wavenumber $k(\mathbf{x})$ in the above Helmholtz equation. Additionally, the potential $V(\mathbf{x})$ is often decaying in function of growing $\mathbf{x}$. These observations will prove particularly valuable in the context of this paper.

2.4. The single and double ionization regimes

We now briefly expound on the physical interpretation of the 2D Schrödinger system (7) in which V_1 and V_2 are assumed to be identical one-body potentials, which describe the attraction (repulsion) to the central nucleus, and V_{12} is a two-body potential, which describes the mutual attraction (repulsion) between the two scattered particles. Depending on the strength of the one-body potentials V_1 and V_2 and the energy E, the problem allows for so-called single ionization waves, which are localized evanescent waves that propagate along the edges of the domain, see Figure 1(a). If the attraction of V_1 is strong enough, there exists a one-dimensional eigenstate $\phi_n(x)$ with a negative eigenvalue $\lambda_n < 0$, characterized by the one-dimensional Helmholtz equation

$$\left(-\frac{1}{2}\frac{d^2}{dx^2} + V_1(x)\right)\phi_n(x) = \lambda_n\, \phi_n(x), \quad \text{for } x \geq 0. \tag{9}$$

Note that $\phi_n(0) = 0$ and $\phi_n(x \to \infty) = 0$. If the two-body potential $V_{12}(x, y)$ is negligibly small, then there automatically also exists a bound state of the 2D system, since each state $\phi_n(x)\phi_n(y)$ is an eigenstate of the separable Hamiltonian $(-1/2)\Delta + V_1(x) + V_2(y)$ with eigenvalue $2\lambda_n$. In the presence of a small but non-negligible two-body potential, this eigenstate will be slightly perturbed, resulting in an eigenstate $\phi_n(x, y)$ with eigenvalue μ_n that fits the 2D subsystem

$$\left(-\frac{1}{2}\Delta + V_1(x) + V_2(y) + V_{12}(x, y)\right)\phi_n(x, y) = \mu_n \phi_n(x, y), \quad x, y \geq 0. \tag{10}$$

The corresponding eigenvalue is $\mu_n \approx 2\lambda_n < \lambda_n < 0$. This ordering is typical for realistic atomic and molecular systems [3]. Assuming that the potentials are such that $\mu_n < \lambda_n < 0$, there are three possible regimes of interest in equation (7), depending on the total energy E. First, for $E < \lambda_n$, the problem is easy to solve numerically, but no interesting physical reactions occur, since there are no scattering states in the solution. For energy levels $\lambda_n < E < 0$, single ionization scattering occurs, i.e. there are scattering solutions that are localized along one of the two axes in the 2D domain, see Figure 1(a). These solutions take the form $\phi(y)\phi_n(x)$ as $y \to \infty$, where $\phi_n(x)$ is the eigenstate of (9) and $\phi(y)$ is a scattering solution satisfying outgoing wave boundary conditions, and vice versa for the permuted coordinates. For energies $E > 0$, both single and double ionization occurs simultaneously. The solution contains – besides single ionization waves – double ionization waves, see Figure 1(b). These are waves that describe a 2D quantum mechanical system that is fully broken up into all its sub-particles. In this case, both relative coordinates x and y can become large, resulting in a 2D scattered wave that extends over to the entire domain.

Note that the principles outlined above can be directly extended to the three-particle system (6) with $d = 3$. For energies $E > 0$ the solution then contains triple ionization waves in addition to the single and double ionization waves described above, which simulate the full break-up of the 3D partial wave system.

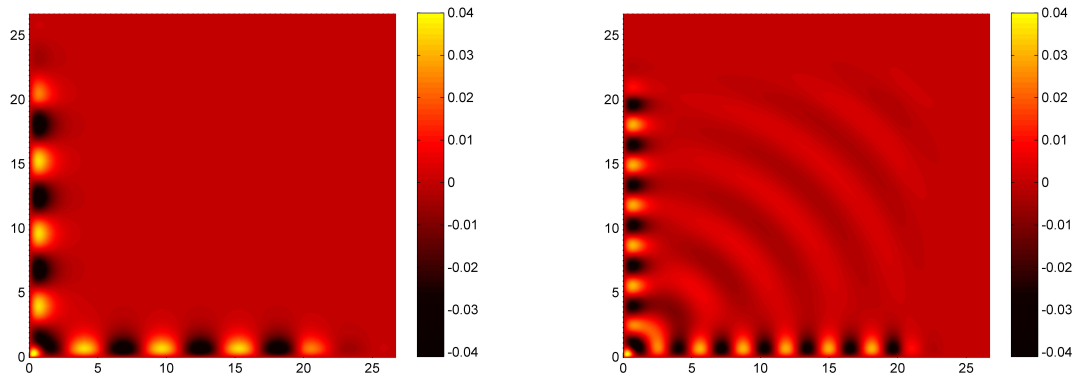

(a) Single ionization

(b) Double ionization

Figure 1: Scattered wave solutions $u(x, y)$ to model problem (7). Model specifications: finite difference discretization on the domain $\Omega = [0, 20]^2$ using $n_x \times n_y = 400 \times 400$ grid points (+ 150 points per dimension in the ECS absorbing layer). Exponential potentials $V_1(x) = -4.5\exp(-x^2)$, $V_2(y) = -4.5\exp(-y^2)$ and $V_{12}(x, y) = 2\exp(-(x + y)^2)$ and right-hand side $f(x, y) = \exp(-3(x + y)^2)$. (a): Solution for energy $E = -0.4$ for which only single ionization occurs. Single ionization waves are localized bound states travelling along the edges of the domain. (b): Solution for energy $E = 1$ for which both single and double ionization occur, resulting in the existence of waveforms along the edges as well as in the middle of the domain.

2.5. The far field map: classical computation and properties

In physical experiments differential cross sections are measured by detecting the fragments that emerge from the break-up problem. These cross sections are probability distributions describing the probability of the particle emerging with a certain energy in a certain direction after the break-up. Since in practical applications the distance from the target to the detector is much larger than the size of the system, the measured cross sections are in fact far field maps of the scattered wave solution. The numerical calculation of the far field map is a two-step process, as outlined in detail below.

Step 1. First the Schrödinger equation (6) – or equivalently the Helmholtz equation (8) – is discretized, meaning the solution is represented on a finite numerical grid and the differential operators are represented by algebraic matrix operators. Unless explicitly stated, we generally use an equidistant, dimension-uniform discretization, where the number of grid points per spatial dimension is denoted by n_x, n_y, ..., respectively. The infinite domain $\mathbb{R}^d$ is replaced by a finite domain $\Omega \subset \mathbb{R}^d$ using absorbing boundary conditions or absorbing layers, implemented using e.g. Perfectly Matched Layers (PML) [4] or Exterior Complex Scaling (ECS) [23]. For a total of $N = n_x \times n_y$ grid points, the discretization of the Schrödinger equation (6) results in a large and sparse linear system of the form

$$\sum_{j=1}^{N} \left(-\frac{1}{2} \left(\Delta^h\right)_{ij} + (V)_{ij} - E\delta_{ij} \right) u_j^N = f_i, \quad i = 1, \ldots, N, \tag{11}$$

where $\left(\Delta^h\right)_{ij}$ is the discrete representation of the Laplacian, which is sparse and typically depends on a discretization parameter h, $(V)_{ij}$ is the representation of the potential, which is often diagonal, and u_j and f_i are the grid representations of the solution and the right-hand side respectively. The construction of $\left(\Delta^h\right)$ in the presence of an absorbing boundary layer is discussed in [2]. In the first step of the classical far field map calculation the linear system (11) is then solved resulting in the numerical solution u^N. Due to the incorporation of absorbing boundary conditions the system may no longer be Hermitian but rather complex symmetric. The spectral properties of the operator $\left(\Delta^h\right)$ for a finite difference discretization with an ECS absorbing layer are discussed in Reps et al. [27], and are further commented on in Section 3.4 of this paper. The resulting linear system (11) is indefinite and is hence very hard to solve using iterative methods such as multigrid preconditioned Krylov subspace methods, the traditional method of choice for large and sparse linear systems [15].

Step 2. The second step extracts the far field map from the numerical scattered wave solution u^N to equation (11). Indeed, solving (11) yields the numerical solution inside a bounded discretization box. However, in practice only the probability distribution far away from the object is measured. An additional post-processing step is hence required to translate the numerical solution of Step 1 into the far field map. The extraction of the far-field map is explained on the continuous equation. Splitting the potential V in one-body and two-body operators, see (2), allows us to rewrite the Schrödinger equation (6) as

$$\left(-\frac{1}{2}\Delta + \bar{V}_1(\mathbf{x}) - E\right) u(\mathbf{x}) = f(\mathbf{x}) - \bar{V}_2(\mathbf{x})u(\mathbf{x}), \qquad \text{for } \mathbf{x} \in \mathbb{R}^d.$$

For separable potentials such as the one-body potentials, an explicit analytical expression exists which satisfies $\left(-\frac{1}{2}\Delta + \bar{V}_1(\mathbf{x}) - E\right) G(\mathbf{x}, \mathbf{y}) = \delta(\mathbf{x} - \mathbf{y})$. The fundamental solution $G(\mathbf{x}, \mathbf{y})$ is called the Green's function, and it allows to write the solution u in any point $\mathbf{x} \in \mathbb{R}^d$ as an integral

$$u(\mathbf{x}) = \int_{\mathbb{R}^d} G(\mathbf{x}, \mathbf{y}) \left(f(\mathbf{y}) - \bar{V}_2(\mathbf{y})u(\mathbf{y})\right) d\mathbf{y}, \qquad \text{for } \mathbf{x} \in \mathbb{R}^d. \tag{12}$$

This integral can effectively be calculated by substituting the numerical solution u^N to the linear system (11) obtained in Step 1 into the integrand in (12), i.e.

$$u(\mathbf{x}) = \int_{\Omega} G(\mathbf{x}, \mathbf{y}) \left(f(\mathbf{y}) - \bar{V}_2(\mathbf{y})u^N(\mathbf{y})\right) d\mathbf{y}, \qquad \text{for } \mathbf{x} \in \mathbb{R}^d. \tag{13}$$

This approach has been successfully used to solve challenging break up problems, see [9, 20, 23].

Remark 1. Note that in the above exposition on the far field map it is assumed that both the source term $f(\mathbf{y})$ and the potential $\bar{V}_2$ are compactly supported. This assumption is used when computing the numerical solution u^N to the system (11) on a bounded numerical domain Ω that covers the support of f and $\bar{V}_2$, and consequently using this solution in the restriction of the integral (13) to the domain Ω.

3. The complex contour approach for far field map calculation

The traditional far field map calculation is generally not scalable to very large, high-dimensional multiparticle problems due to the main computational bottleneck that lies in solving the linear system (11). This system has similar properties to the indefinite Helmholtz problem that appears in e.g. seismic inversion [29]. The construction of efficient solvers for the indefinite Helmholtz system is still an open and active research topic within the applied mathematics community. However, since we are in fact not interested in the numerical solution u^N to (11) itself, but rather in the far field map of this solution, i.e. a Green's integral over u^N, the actual path of integration can be deformed. This gives additional freedom in the development of the solution method.

3.1. Deforming the far field integral

In [10] an efficient method for the computation of the far field map for indefinite Helmholtz problems was proposed. It was suggested that if f and $\bar{V}_2$ are analytical functions, the integral in equation (13) can alternatively be evaluated along a complex contour $Z \subset \mathbb{C}^d$, i.e.

$$u(\mathbf{x}) = \int_{Z} G(\mathbf{x}, \mathbf{z}) \left(f(\mathbf{z}) - \bar{V}_2(\mathbf{z})u(\mathbf{z})\right) d\mathbf{z}, \tag{14}$$

rather than the physical real-valued domain $\Omega \subset \mathbb{R}^d$. The complex-valued domain Z is illustrated schematically for the 1D case in Figure 2. The illustrated complex contour grid can be readily extended to d dimensions through the use of Kronecker products. Note that the integral over the subdomain Z_2 vanishes; hence, the integral (14) is in fact only evaluated along the complex rotated grid $Z_1 = \{\mathbf{z} = \mathbf{x}e^{i\gamma} : \mathbf{x} \in \Omega \subset \mathbb{R}^d\}$.

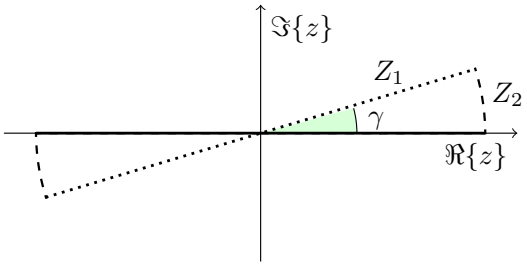

Figure 2: Schematic representation of the complex contour for the far field integral calculation (14) illustrated in 1D. The full line represents the real-valued computational domain Ω, the dotted and dashed lines represent the complex-valued subdomains $Z_1 = \{\mathbf{x}e^{i\gamma} : x \in \Omega \subset \mathbb{R}\}$ and $Z_2 = \{be^{i\theta} : b \in \partial\Omega,\ \theta \in [0, \gamma]\}$ of the complex contour.

The far field map computation from the complex formulation (14) now requires the Schrödinger equation (6) to be solved along a complex-valued contour in order to obtain $u(\mathbf{z})$ for $\mathbf{z} \in Z$. It was shown in the literature that the spectral properties of the corresponding Schrödinger operator discretized along the complex contour are favorable for iterative solution [14, 27]. Indeed, equation (6) is reduced to a damped equation along the contour, which is much more amenable to iterative solution, particularly using multigrid. A key requirement for the validity of the complex contour integral reformulation (14) is the observation that the potentials appearing in the context of quantum mechanical break-up problems are continuous functions everywhere in the domain except at the exact nuclear positions. This is in contrast to many engineering and seismic problems, where the wavenumber (potential) often represents objects that exhibit material jumps (discontinuities).

Remark 2. Note that the deformation of the integrating domain (14) is only valid for analytical functions f and $\bar{V}_2$, which seemingly contradicts the earlier assumption that f and $\bar{V}_2$ are compactly supported, see Section 2.5. The far field map computation in Section 2.5 can however be extended to the more general class of analytical functions f and $\bar{V}_2$ that vanish at infinity. Indeed, using smooth bump functions [19, 25], functions with compact support can be shown to be dense within the space of functions that vanish at infinity. Consequently, every analytical function can be arbitrarily closely approximated by a series of compactly supported functions, which in turn implies that the corresponding Helmholtz solutions on a limited computational domain can be arbitrarily close to the solution of the Helmholtz equation generated with the analytical vanishing function. This means that if f and $\bar{V}_2$ are analytical but sufficiently small everywhere outside $\Omega \subset \mathbb{R}^d$, the computational domain for the integral (13) may be truncated to the numerical domain Ω as if f was compactly supported. Hence, (13) is well-defined for analytical functions f and $\bar{V}_2$ that vanish at infinity, and the deformation to (14) is valid.

Remark 3. The supposition that both the source function and the two-body potentials are exponentially decaying is a natural assumption in the context of photoionization problems. Hence, for photoionization, the complex integral (14) is well-defined and directly yields the ionization cross section. However, when modeling electron impact problems, the integral should generally be split into two parts: one real-valued integral over the right-hand side f along the real domain Ω, and one complex-valued integral over the scattered wave along the complex domain Z, i.e.

$$u(\mathbf{x}) = \int_{\Omega} G(\mathbf{x}, \mathbf{y})\, f(\mathbf{y})\, d\mathbf{y} - \int_{Z} G(\mathbf{x}, \mathbf{z})\, \bar{V}_2(\mathbf{z}) u(\mathbf{z})\, d\mathbf{z}. \tag{15}$$

Note that for the left-most integral, the integrand is known explicitly. The motivation for this splitting originates from the fact that for electron impact models, like the 2D Temkin-Poet model (see Section 5), the incoming wave $u_{\text{in}}(x, y) = \phi_n(x) \sin(k_n y)$ acts as a source term in the right-hand side $f(x, y) = (V_1(x) + V_{12}(x, y))\, u_{\text{in}}(x, y)$. Here $k_n = \sqrt{2(E - \lambda_n)}$ and ϕ_n is an eigenstate of the one-body operator (9) with negative eigenvalue λ_n. The function $\sin(k_n y)$ is exponentially increasing along the complex contour,

whereas the potentials typically decrease only linearly. This implies the right-hand side f does not vanish at infinity for impact ionization problems. Hence the integral over f cannot be evaluated along the complex contour and must be treated separately as a real-valued integral instead.

Note that splitting the integral as suggested above has one important technical consequence. When summing up the real- and complex-valued integrals in (15), the normalization for the 1D eigenstates ϕ_n has to be chosen consistently.[1] Hence, we propose to use the alternative normalization $\int_0^\infty \phi(z)^2 dz = 1$ for the eigenstates ϕ in this work, rather than the more commonly used Hermitian inner product with complex conjugation. In this way the complex-valued eigenmodes are normalized identically to the normalization on the real-valued domain where the Hamiltonian is Hermitian.

3.2. The complex contour approach: proof of concept

We briefly recapitulate some of the key results from our previous work [10], where the applicability of the complex contour method on 2D and 3D Schrödinger equations describing a quantum mechanical scattering problem was validated.

Consider a 2D ($d = 2$) Helmholtz equation of the form (8) with source function $g(\mathbf{x}) = (k^2(\mathbf{x}) - k_0^2)\, u_{\text{in}}(\mathbf{x})$. The equation is discretized using second order finite differences on an n^d-point uniform Cartesian mesh covering a square numerical domain $\Omega = [-20, 20]^d$. The space-dependent wavenumber is

$$k^2(x, y) = k_0^2 - 1/5 \left(e^{-((x+2)^2+(y-4)^2)} + e^{-((x-2)^2+(y+4)^2)} \right), \quad (x, y) \in [-20, 20]^2, \tag{16}$$

i.e. the object of interest takes the form of two circular point-like objects with mass concentrated at the Cartesian coordinates $(2, -4)$ and $(-2, 4)$, see Figure 3 (top panel). The incoming wave scattering at the given object is defined by

$$u_{\text{in}}(\mathbf{x}) = e^{ik_0 \boldsymbol{\eta} \cdot \mathbf{x}}, \quad \mathbf{x} = (x, y) \in \Omega,$$

where $\boldsymbol{\eta}$ is the unit vector in the x-direction. The far field amplitude is given by the integral

$$F(\boldsymbol{\alpha}) = \int_\Omega e^{-ik_0 \mathbf{x} \cdot \boldsymbol{\alpha}} \left[g(\mathbf{x}) + (k^2(\mathbf{x}) - k_0^2)\, u^N(\mathbf{x}) \right] d\mathbf{x}, \tag{17}$$

where $\boldsymbol{\alpha}$ is the outgoing wave unit vector. Figure 3 illustrates the equivalence between the classical real-valued far field map integral and the complex contour formulation. The 2D Helmholtz model problem with wavenumber given by (16) and $k_0 = 1$ is solved for u^N using, respectively, a standard LU factorization method on the real domain Ω with ECS boundary layers ($\theta_{ECS} = \pi/4$) along the domain boundary $\partial\Omega$, and a series of multigrid V(1,1)-cycles with ω-Jacobi smoothing on the full complex domain ($\gamma = 14.6°$) with a residual reduction tolerance of `1e-6`. The standard multigrid intergrid operators used are bilinear interpolation and full weighting restriction. The moduli of the wavenumber contrast function $k^2(\mathbf{x}) - k_0^2$ (top) and the resulting solution u^N (mid) are shown on Figure 3 for both methods. Note how the solution u^N on the full complex contour (right) is heavily damped compared to the solution on the real domain (left). Consequently, using the numerical solution u^N, the 2D far field map integral (17) can be calculated using any numerical integration scheme over the real or complex domain respectively. The resulting far field map $F(\boldsymbol{\alpha})$ is shown as a function of the outgoing wave direction $\boldsymbol{\alpha}$ on Figure 3 (bottom). One observes that the mapping is indeed identical when calculated over the real-valued (left) and complex-valued (right) domain. However, the computational cost of the real-domain method for calculation of the far field map is significantly reduced by the ability to apply a multigrid method to the complex scaled problem.

[1] For completeness, note that the eigenstates ϕ_n are a factor of u_{in} in the real-valued part of the integral (15); however, ϕ_n also intrinsically appears in the complex-valued integral over the scattered wave as part of the right-hand side of equation (11).

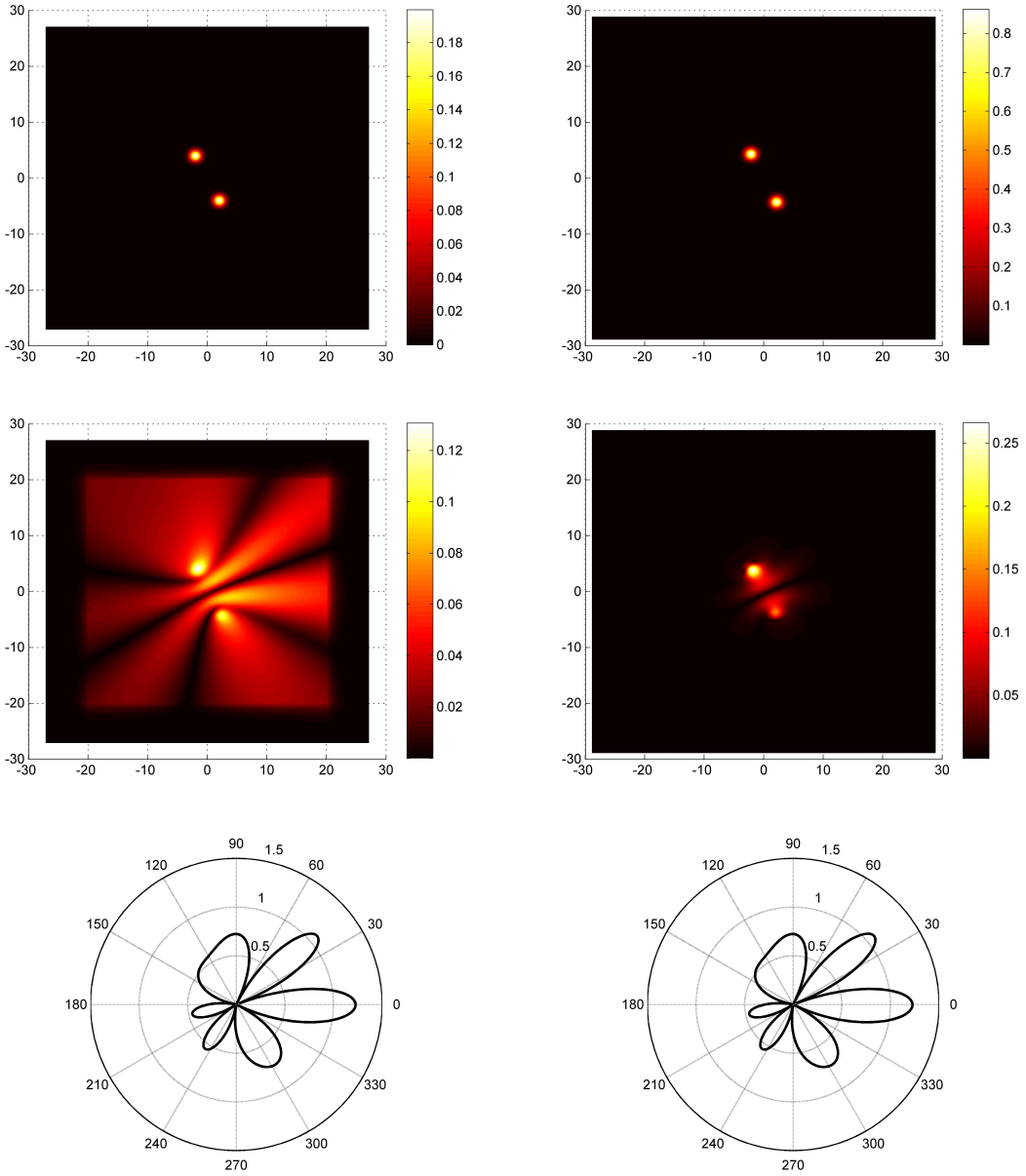

Figure 3: Comparison between the classical real-valued far field map calculation (left) and the complex-valued approach (right). Top: 2D object contrast function $|k^2(\mathbf{x}) - k_0^2|$ given by (16). Mid: solutions to the Helmholtz problem (8) (modulus) on an $n_x \times n_y = 256 \times 256$ grid. Real-valued problem (incl. double ECS contour with $\theta_{ECS} = \pi/4$) solved using LU factorization; complex-valued problem solved using a series of multigrid V-cycles with ω-Jacobi smoother on a full complex contour with $\gamma = 14.6°$ (residual reduction tolerance `1e-6`). Bottom: 2D Far field maps $F(\boldsymbol{\alpha})$ for both approaches.

3.3. The ionization cross sections

In practice, the far field maps of (10) are Green's integrals over the solution, see [23]. Indeed, for a 2D problem setting where $\mathbf{x} = (x, y)$, the single ionization amplitude $s_n(E)$, which represents the probability of particle single ionization, is given by

$$s_n(E) = \int_\Omega \phi_{k_n}(x)\phi_n(y)\left[f(x,y) - V_{12}(x,y)u(x,y)\right]\, dx\, dy, \tag{18}$$

where $k_n = \sqrt{2(E - \lambda_n)}$. Here the function ϕ_n is a one-body eigenstate, i.e. a solution of equation (9) with corresponding eigenvalue λ_n, and the function ϕ_{k_n} is a regular, normalized solution of the homogeneous

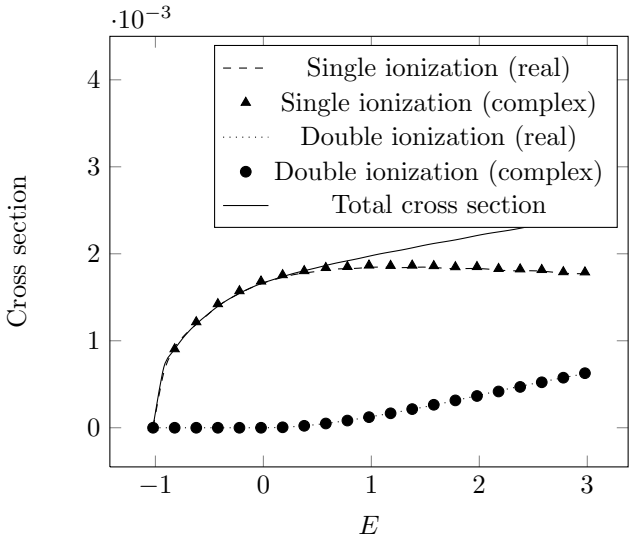

Figure 4: Comparison of the single and double ionization total cross sections calculated using the numerical scattered wave solution u^N to (7). Computation performed on (a) a traditional real-valued ECS grid with $\theta_{ECS} = 25.7°$ and (b) a full complex contour with $\gamma = 8.5°$. The energy range starts at the single ionization threshold $E = -1$, corresponding to a strictly positive cross section. Double ionization occurs for energy levels $E > 0$.

Helmholtz equation

$$\left(-\frac{1}{2}\frac{d^2}{dx^2} + V_1(x) - \frac{1}{2}k^2\right)\phi_k = 0, \tag{19}$$

where $k = k_n$ and ϕ_{k_n} is normalized by $1/\sqrt{k_n}$. Similarly, the double ionization cross section $\zeta(k_1, k_2)$, which measures the probability of double ionized particles, is defined by the integral

$$\zeta(k_1, k_2) = \int_\Omega \phi_{k_1}(x)\phi_{k_2}(y)\left(f(x,y) - V_{12}(x,y)u(x,y)\right)\,dx\,dy, \quad x, y \geq 0, \tag{20}$$

where both $\phi_{k_1}(x)$ and $\phi_{k_2}(y)$ are solutions to (19), with $k_1 = \sqrt{2E}\sin(\alpha)$ and $k_2 = \sqrt{2E}\cos(\alpha)$, respectively, and $\alpha \in [0, \pi/2]$ such that $k_1^2 + k_2^2 = 2E$. The total double ionization cross section is defined as the integral

$$\sigma_{tot}(E) = \int_0^E \sigma(\sqrt{2\epsilon}, \sqrt{2(E-\epsilon)})\,d\epsilon, \tag{21}$$

where

$$\sigma(k_1, k_2) = \frac{8\pi^2}{k_0^2}\frac{1}{k_1 k_2}|\zeta(k_1, k_2)|^2.$$

Note that the cross section integral expressions (18) and (20) are effectively of the form (13), i.e. these are far field maps of the Schrödinger solution $u(x, y)$, and the complex contour approach is hence applicable.

Figure 4 shows the rate of single and double ionization as a function of the total energy E for a 2D Schrödinger model of the form (7) with source term $f(x, y) = \exp(-3(x + y)^2)$. The potentials are exponential functions defined as $V_1(x) = -4.5\exp(-x^2)$, $V_2(y) = -4.5\exp(-y^2)$ and $V_{12}(x, y) = 2\exp(-(x + y)^2)$. The dashed and dotted lines on Figure 4 represent the total single and double ionization amplitudes calculated using the traditional real-valued method with ECS absorbing boundary conditions [23]. The corresponding 2D scattering problem (7) is solved on a numerical domain $\Omega = [0, 15]^2$ covered by a finite difference grid consisting of 300 grid points per spatial dimension. An ECS absorbing boundary layer of 150 additional grid points per dimension starting at $x = 15$ ($y = 15$ resp.) simulates the outgoing wave boundary conditions for $x \to \infty$ and $y \to \infty$ ($\theta_{ECS} = \pi/7 \approx 25.7°$). Equivalent results obtained using the complex contour approach are indicated by the ▲ and • symbols on Figure 4. The Schrödinger equation (7) is first solved on a complex contour, yielding a damped solution, followed by the calculation of the integrals (18) and (20) along the complex domain. A complex scaled grid with an overall complex rotation angle $\gamma = \pi/21 \approx 8.5°$ is used.

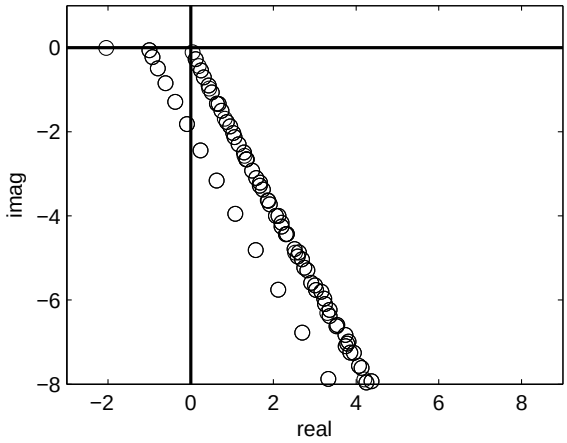

Figure 5: Spectrum (close-up) of the discretized 2D Hamiltonian (22) on a complex contour with grid distance $he^{-i\gamma}$, where $h = L/n_x = L/n_y$ is the corresponding real-valued grid distance with domain length L. The complex grid rotation angle is $\gamma = \pi/6$, causing the spectrum to be rotated down into the complex plane over an angle $2\gamma = \pi/3$.

3.4. Spectral properties of the 2D Schrödinger operator

To obtain additional insight in the multigrid convergence, we briefly discuss the spectral properties of the discretized 2D Schrödinger operator. The discretized 2D Hamiltonian H^{2d} corresponding to equation (7) can be written as a sum of two Kronecker products and a two-body potential, i.e.

$$H^{2\mathrm{d}} = H_1 \otimes I + I \otimes H_2 + V_{12}(x, y), \tag{22}$$

where

$$H_1 = -1/2\Delta + V_1 \qquad \text{and} \qquad H_2 = -1/2\Delta + V_2$$

are the discretized one-dimensional Hamiltonians. When the two-body potential $V_{12}(x, y)$ is weak relative to the one-body potentials $V_1(x)$ and $V_2(y)$, the eigenvalues of the 2D Hamiltonian H^{2d} can be approximated by

$$\lambda^{2\mathrm{d}} \approx \lambda_1 + \lambda_2,$$

where $H_1\phi(x) = \lambda_1\phi(x)$ and $H_2\phi(y) = \lambda_2\phi(y)$. The spectrum of the one-dimensional Hamiltonians H_1 and H_2 closely resembles the spectrum of the 1D Laplacian $(-1/2)\Delta$; however, the presence of the potential modifies the smallest eigenvalues, typically yielding a single (or a small number of) negative eigenvalue(s) due to the attractive potential.

The spectrum of the complex rotated 2D Schrödinger operator with $E = 0$ is shown on Figure 5. The eigenvalues of the 2D Hamiltonian are rotated down in the complex plane when the system is discretized along a complex-valued contour. An isolated negative real eigenvalue at -2.043 appears, and two series of eigenvalues emerge from the real axis at -1.012 and 0 respectively. The leftmost branch of eigenvalues originates from the sum of the negative eigenvalue of the first 1D Hamiltonian H_1 combined with all the positive eigenvalues of the second 1D Hamiltonian H_2, and vice versa. The second series of eigenvalues starting at the origin is approximately formed by the sums of the positive eigenvalues of both one-dimensional Hamiltonians. The isolated eigenvalue is a bound state of H^{2d}. The leftmost branch correspond to so-called single-ionization states, i.e. highly oscillatory localized 1D waveforms propagating close to the $x = 0$ and $y = 0$ axes.

Depending on the sign of the energy E, the spectral properties of the system to be solved change. Its spectrum is then composed of the eigenvalues of H^{2d}, shown in Fig. 5, shifted to the left or right. For some negative energies $E < 0$ (single ionization regime), this might result in an eigenvalue located close to zero, which causes most iterative solvers (including multigrid) to suffer from a severe convergence slow down. This observation forms the major motivation for the development of an additional correction scheme to support the multigrid solver. The Coupled Channel Correction Scheme introduced in the next section is designed specifically to account for the bound state eigenmodes.

4. MG-CCCS: a multigrid-based solver which includes a Coupled Channel Correction Scheme

It was shown in [10] that multigrid generally acts as an efficient solution scheme for the discretized Schrödinger system (11) when the latter is represented along a complex contour. However, it was also observed that multigrid convergence tends to stagnate for energies $E < 0$. Notably, a deterioration in convergence occurs when the problem is not fully broken up in its subparticles, in which case the convergence rate is strongly affected by the presence of eigenvalues near the real axis on both sides of the origin, cf. Section 3.4.

In this section, we present a correction scheme that can be used in addition to the standard multigrid scheme, and which is designed specifically at resolving the low-dimensional single ionization waves in the solution. Using the Coupled Channel approximation [18, 22] we obtain a system of $(d-1)$-dimensional Coupled Channel equations, which can be solved directly due to the dimension reduction, and can consequently be used to correct the solution. The separate handling and elimination of the bound states from the error results in an overall more robust iterative solution scheme. We derive the Coupled Channel scheme in a 2D problem setting for notational and implementation convenience.

4.1. The Coupled Channel approximation

The aim of the correction scheme is to approximately solve the driven Schrödinger equation

$$(H - E)\, u(x,y) = (H_1 + H_2 + V_{12}(x,y) - E)\, u(x,y) = f(x,y) \tag{23}$$

for an energy E where single ionization waves dominate the solution. This implies that, in large parts of the domain, the solution can be written as the product of an outgoing wave in one coordinate with an eigenstate in the other coordinate. Let us assume that the 1D Hamiltonians H_1 and H_2 are such that there are eigenstates

$$H_1\phi_n(x) = \lambda_n\phi_n(x),$$

$$H_2\varphi_n(y) = \mu_n\varphi_n(y),$$

with $\lambda_n < 0$ and $\mu_n < 0$. Using the so-called Coupled Channel approximation, we approximate a given function $u(x,y)$ as

$$u(x,y) \approx \sum_{m=1}^{M} A_m(y)\phi_m(x) + \sum_{l=1}^{L} B_l(x)\varphi_l(y), \tag{24}$$

where M and L are assumed to be much smaller that the number of discretization points in each respective spatial dimension. The coefficient functions A_m and B_l can represent, for example, the asymptotic form of a single ionization outgoing wave, for which it is known that $\lim_{y\to\infty} u(x,y) = \sum_{m=1}^{M} S_m \exp(ik_m y)\phi_m(x)$, where S_m are the single ionization amplitudes and $k_m = \sqrt{2(E-\lambda_m)}$.

Remark 4. Note that the approximate expansion (24) is generally not uniquely defined. Indeed, we can add arbitrary linear combinations of the eigenfunctions $\varphi_l(y)$ to $A_m(y)$ without modifying the approximation.

For example, adding $\sum_{l=1}^{L} \alpha_{lm}\varphi_l(y)$ to $A_m(y)$ is compensated by subtracting a similar linear combination of the eigenmodes $\phi_m(x)$ from $B_l(x)$, i.e.

$$\sum_{m=1}^{M}\left(A_m(y)+\sum_{l=1}^{L}\alpha_{lm}\varphi_l(y)\right)\phi_m(x)+\sum_{l=1}^{L}\left(B_l(x)-\sum_{m=1}^{M}\alpha_{lm}\phi_m(x)\right)\varphi_l(y)$$
$$=\sum_{m=1}^{M}A_m(y)\phi_m(x)+\sum_{l=1}^{L}B_l(x)\varphi_l(y).$$

To define a unique representation of the form (24), we choose, without loss of generality, $A_m(y)$ and $B_l(x)$ such that (for $1 \le i \le M$, $1 \le j \le L$)

$$a_{ji} := \int_0^\infty A_i(y)\varphi_j(y)dy = 0, \qquad \forall j > i, \tag{25}$$

$$b_{ij} := \int_0^\infty B_j(x)\phi_i(x)dx = 0, \qquad \forall i \ge j. \tag{26}$$

Note, however, that any other convention, for example that all $a_{ji} = 0$ for all i, j, would also be possible.

Given a known function $u(x, y)$ we can now calculate the corresponding coefficient functions $A_m(y)$ and $B_l(x)$ of the Coupled Channel approximation as follows. For $1 \le i \le M$ and $1 \le j \le L$, it holds that

$$A_i(y)=\int_0^\infty u(x,y)\phi_i(x)dx-\sum_{l=1}^{L}\left(\int_0^\infty B_l(x)\phi_i(x)dx\right)\varphi_l(y)=\int_0^\infty u(x,y)\phi_i(x)dx-\sum_{l=1}^{L}b_{il}\varphi_l(y),$$

$$B_j(x)=\int_0^\infty u(x,y)\varphi_j(y)dy-\sum_{m=1}^{M}\left(\int_0^\infty A_m(y)\varphi_j(y)dy\right)\phi_m(x)=\int_0^\infty u(x,y)\varphi_j(y)dy-\sum_{m=1}^{M}a_{jm}\phi_m(x).$$

Hence, the coefficients a_{ji} and b_{ij} need to be computed in order to calculate $A_i(y)$ and $B_j(x)$. These are found directly from $u(x, y)$ by integration, since

$$\int_0^\infty\int_0^\infty \phi_i(x)\varphi_j(y)\,u(x,y)\,dxdy = a_{ji} + b_{ij}. \tag{27}$$

Since b_{ij} is zero while a_{ji} is non-zero and vice versa due the uniqueness conventions (25)-(26), the coefficients a_{ji} and b_{ij} are indeed uniquely defined by (27), and hence the expansion (24) can be computed.

4.2. The Coupled Channel projection space

Given the 2D driven Schrödinger equation, we now represent both the unknown solution and the known right-hand side in a factorized way using the Coupled Channel approximation (24). Equation (23) becomes

$$(H_1+H_2+V_{12}(x,y)-E)\left(\sum_{m=1}^{M}A_m(y)\phi_m(x)+\sum_{l=1}^{L}B_l(x)\varphi_l(y)\right)=\sum_{m=1}^{M}f_m^A(y)\phi_m(x)+\sum_{l=1}^{L}f_l^B(x)\varphi_l(y),$$

where f_m^A and f_l^B are uniquely defined, cf. (25)-(26), and can be calculated explicitly. A decomposition of this equation gives rise to a pair of coupled systems of equations. The first system is found by starting from

$$(H_1+H_2+V_{12}(x,y)-E)\left(\sum_{m=1}^{M}A_m(y)\phi_m(x)\right)=\sum_{m=1}^{M}f_m^A(y)\phi_m(x).$$

Using the fact that $H_1\phi_n(x) = \lambda_n\phi_n(x)$, multiplying the above equation with $\phi_i(x)$ (for $1 \le i \le M$) and integrating over x yields

$$(H_2+\lambda_i-E)\,A_i(y)+\sum_{m=1}^{M}\left(\int_0^\infty V_{12}(x,y)\phi_i(x)\phi_m(x)dx\right)A_m(y)=f_i^A(y).$$

Note that we use a specific normalization of the eigenmodes in order to obtain the above equation.[2] Introducing the notation $V^A_{im}(y) := \int_0^\infty V_{12}(x,y)\phi_i(x)\phi_m(x)dx$ $(1 \le i,m \le M)$, this ultimately results in the Coupled Channel equation for $A_i(y)$

$$\left(H_2 + \lambda_i + V^A_{ii}(y) - E\right) A_i(y) + \sum_{\substack{m=1 \\ m\neq i}}^{M} V^A_{im}(y) A_m(y) = f^A_i(y) \quad \text{for} \quad i = 1,\ldots,M. \tag{28}$$

In a similar way, one can derive a coupled system for $B_j(x)$

$$\left(H_1 + \mu_j + V^B_{jj}(x) - E\right) B_j(x) + \sum_{\substack{l=1 \\ l\neq j}}^{L} V^B_{jl}(y) B_l(x) = f^B_j(y) \quad \text{for} \quad j = 1,\ldots,L, \tag{29}$$

where $V^B_{jl}(y) := \int_0^\infty V_{12}(x,y)\varphi_j(y)\varphi_l(y)dy$ $(1 \le j,l \le L)$. These equations are known as the Coupled Channel equations and are frequently used to describe electronic states in atoms and molecules, see [16].

For the 2D Schrödinger system (23) the corresponding Coupled Channel equations (28)-(29) form a set of $M+L$ one-dimensional equations that need to be solved in order to obtain the Coupled Channel representation (24) for the solution $u(x,y)$. Hence, the Coupled Channel approximation can be considered as a dimension reducing projection of the 2D solution $u(x,y)$ onto a collection of 1D subproblems.

4.3. The Coupled Channel Correction Scheme

We now use the Coupled Channel equations (28)-(29) to define a correction scheme for the solution of the driven Schrödinger equation. Let $u^{(k)}(x,y)$ be a k-th guess for the solution of equation (23), which was computed by some iterative solution scheme (e.g. a series of multigrid V-cycles) from a previous guess $u^{(k-1)}(x,y)$. An improved guess $u^{*(k)}$ can be obtained with the help of the following correction scheme. We first formulate the error equation

$$(H - E)\, e^{(k)}(x,y) = r^{(k)}(x,y),$$

where $e^{(k)}(x,y) = u(x,y) - u^{(k)}(x,y)$ is the current guess error and $r^{(k)} = f(x,y) - (H-E)\, u^{(k)}(x,y)$ is the corresponding residual. Instead of solving the error equation exactly, which is as hard as solving the original problem, we solve it approximately using the Coupled Channel approximation (24). We expand the residual and error functions using the Coupled Channel approximation, such that

$$r^{*(k)}(x,y) = \sum_{m=1}^{M} r^A_m(y)\phi_m(x) + \sum_{l=1}^{L} r^B_l(x)\varphi_l(y),$$

$$e^{*(k)}(x,y) = \sum_{m=1}^{M} e^A_m(y)\phi_m(x) + \sum_{l=1}^{L} e^B_l(x)\varphi_l(y).$$

Here, the coefficient functions $r^A_m(y)$ and $r^B_l(x)$ for the residual are known. Subsequently, the Coupled Channel equations are solved for the error coefficient functions $e^A_i(y)$ and $e^B_j(x)$:

$$\left(H_2 + \lambda_i + V^A_{ii}(Y) - E\right) e^A_i(y) + \sum_{\substack{m=1 \\ m\neq i}}^{M} V_{im}(y) e^A_m(y) = r^A_i(y) \quad \text{for} \quad i = 1,\ldots,M,$$

$$\left(H_1 + \mu_j + V^B_{jj}(x) - E\right) e^B_j(x) + \sum_{\substack{l=1 \\ l\neq j}}^{L} V^B_{jl}(y) e^B_l(x) = r^B_j(y) \quad \text{for} \quad j = 1,\ldots,L.$$

[2] Throughout this work we use an alternative normalization of the complex-valued eigenmodes ϕ given by $\int_0^\infty \phi(z)^2 dz = 1$, rather than the more commonly used Hermitian inner product with complex conjugation. See also Remark 3, Section 3.

The solution of these one-dimensional systems is significantly easier than solving the original 2D driven Schrödinger system (23). Indeed, the reduction in spatial dimension allows us to effectively solve the Coupled Channel systems using a direct solution method, which yields a fast and accurate solution. We then correct the current guess for the solution by adding the Coupled Channel approximation of the error $e^{*(k)}(x,y)$ to the current solution $u^{(k)}(x,y)$ as follows

$$\begin{aligned} u^{*(k)}(x,y) &= u^{(k)}(x,y) + e^{*(k)}(x,y) \\ &= u^{(k)}(x,y) + \sum_{m=1}^{M} e_m^A(y)\phi_m(x) + \sum_{l=1}^{L} e_l^B(x)\varphi_l(y). \end{aligned} \tag{30}$$

Remark 5. Note that the extension of the above Coupled Channel Correction Scheme (30) to higher spatial dimensions, notably 3D, can be obtained in an analogous manner. Such a 3D correction scheme would be based upon a double Coupled Channel approximation, introducing corrections for both the 1D and 2D eigenstates to account for the presence of single and double ionization waves travelling along the axes and faces of the coordinate system, respectively. This leads to both 1D and 2D pairs of coupled systems of equations, which are in turn significantly easier to solve than the full 3D break-up problem. Although we believe the generalization to higher dimensions is straightforward, we do not expound on the 3D Coupled Channel Correction Scheme in this work for notational and implementation ease. Instead, we aim to tackle this problem in future work.

5. Implementation and numerical accuracy

Additional care is required for the calculation of the eigenstates involved in the scattering process when the coordinates are rotated into the complex plane. For photoionization problems, the right-hand side is typically the dipole operator applied to the eigenstate with the lowest energy [34]. However, for impact ionization problems the right-hand side contains the incoming wave that consists of a target state, i.e. the eigenstate with the lowest energy, and a purely incoming wave representing the incoming particle [2, 23]. Both of these functions require a careful and accurate numerical description, especially on the complex contour, since after complex rotation the incoming wave becomes an exponentially increasing function.

5.1. The complex contour rotation angle and numerical accuracy

In this section we comment on some key numerical aspects of the proposed complex contour approach. From a theoretical viewpoint the real-valued integral (13) and its counterpart evaluated along the complex contour (14) are identical, independently of the size of the rotation angle γ. Indeed, in principle the rotation angle can be chosen arbitrarily large, implying very strong damping, which is beneficial for the multigrid solver. However, in reality a restriction on the size of the rotation angle is imposed by the numerical implementation. We illustrate this claim on a 2D Temkin-Poet model problem, where it is shown that when the angle of rotation is too large and the potential is long range, significant numerical inaccuracies occur.

5.1.1. The 2D Temkin-Poet model: propagation of round-off errors in the eigenstates

The Temkin-Poet (TP) model is used throughout this work as an approximation to an impact ionization problem, where only s-waves are used to describe the scattered electrons. The model has a long history as a benchmark problem for Schrödinger scattering problems, see e.g. [28], where a two-dimensional TP model was used to describe the impact ionization of molecular hydrogen. Similarly, the impact ionization of helium can be modelled by a 3D Temkin-Poet model [34].

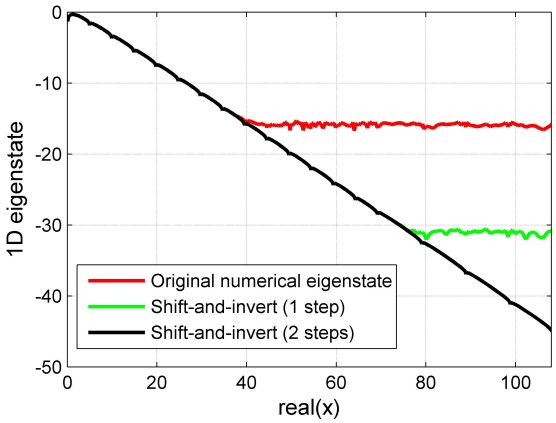

Figure 6: Modulus of the 1D eigenstate $\phi_n(x)$ calculated numerically along the complex contour with $\gamma = 9°$. Plot in function of the real part of the complex-valued x-coordinate. Shown is the numerical eigenstate calculated 'naïvely' using a standard eigenfunction routine (red) and the eigenstate with improved accuracy using several steps of shift-and-invert (green and black). Round-off errors are eliminated after two applications of the shift-and-invert technique. Vertical axis in log-scale.

We consider the 2D Temkin-Poet model discretized using a spectral element type discretization; however, the following observations are independent of the exact discretization scheme. The total wave $u(x, y)$ is the sum of the incoming wave u_{in} and the scattered wave u_{sc}, i.e. $u(x, y) = u_{\text{in}}(x, y) + u_{\text{sc}}(x, y)$. Hence, the far field integral (14) can be effectively split up into a sum of two integrals: one over u_{in} and the other over u_{sc}, see (15). Note that the incoming wave comprises part of the right-hand side in the scattered wave equation (11).

When computing the complex-valued scattered wave for impact-ionization models, some numerical subtleties require specific attention. Notably, the incoming wave is

$$u_{\text{in}}(x, y) = \phi_n(x) \sin(k_n y), \tag{31}$$

with $k_n = \sqrt{2(E - \lambda_n)}$, where ϕ_n is an eigenstate of the one-body operator (9) with a negative eigenvalue λ_n. On the real-valued domain the eigenstate ϕ_n is an exponentially decaying function, since $\lambda_n < 0$ implies that ϕ_n asymptotically behaves as $\exp(\lambda_n x)$. After complex coordinate rotation ϕ_n is still a decaying function. However, when calculated numerically using a standard eigenfunction routine, the exponential decay of ϕ_n is unavoidably truncated at machine precision. This is illustrated in Figure 6, where it is observed that from a certain distance on the exponential decay stagnates at around 1.0^{-16}.

Subsequently the numerical representation of the eigenstate $\phi_n(x)$ is multiplied by $\sin(k_n y)$ to form the incoming wave u_{in}. However, on the complex rotated grid the function $\sin(k_n y)$ becomes an exponentially growing function in y, with the exponential growth being governed by the rotation angle γ. The truncated part of the eigenstate ϕ_n - that should be negligibly small - becomes substantial for larger values of y through the multiplication. Hence, the numerical round-off of the 1D eigenstate ϕ_n produces an unwanted error which propagates through the algorithm.

The incoming wave u_{in} is additionally multiplied by the potentials $V_1(x)$ and $V_{12}(x, y)$ to form the right-hand side of the scattered wave equation (11). The resulting source function is heavily contaminated due to the numerical round-off errors in ϕ_n, as is shown in the left panel of Figure 7. The contaminations at the rightmost (outgoing) domain edges (where both $x \to \infty$ and $y \to \infty$) are due to the numerical round-off error phenomenon described above.

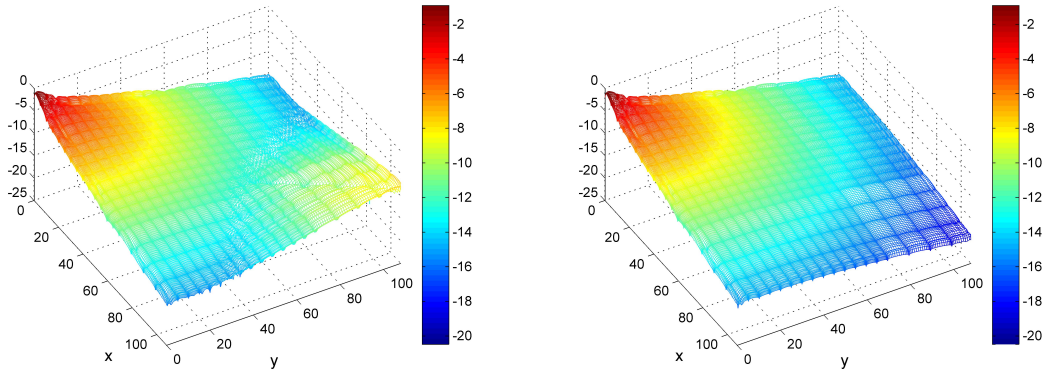

Figure 7: Modulus of the function $(V_1(x) - V_{12}(x,y))\,\phi_n(x)\sin(k_n y)$, which forms the right-hand side of the scattered wave equation (11), calculated numerically on the complex contour with $\gamma = 9°$ for energy $E = 1$. Potentials are $V_1(x) = -\exp(-x^2)$ and $V_{12}(x,y) = \exp(-(x+y)^2)$; comparable results are obtained using Temkin-Poet potentials. Plot in function of the real part of the complex-valued x- and y-coordinates. Vertical axis in log-scale. Left: with standard eigenfunction computation of $\phi_n(x)$. Round-off errors contaminate the function in the region where $80 < x$ and $80 < y$, cf. Figure 6. Right: adapted computation using the iteratively refined eigenstate $\phi_n(x)$. Round-off errors have been eliminated.

5.1.2. Solution to the truncation errors: shift-and-invert

To reduce the numerical inaccuracies due to the round-off of the 1D eigenstates, we apply the classical concept of shift-and-invert [17] to the eigenstate ϕ_n, which is closely related to iterative refinement [36]. This simple iterative update step (power iteration) is based on an additional solve using the shifted Hamiltonians $(H_1 - \lambda_n)$ or $(H_2 - \lambda_n)$, hence allowing for a more accurate representation of the eigenstates ϕ_n. The numerical eigenstate after application of the shift-and-invert technique is shown on Figure 6. Using the improved accuracy of the eigenstates, the round-off errors due to multiplication by the exponentially increasing sine function can be avoided, as illustrated in the right panel of Figure 7. Note that the complex rotation angle γ plays an important role in the numerical accuracy and the avoidance of round-off errors. Even if the numerical accuracy of the eigenstates $\phi_n(x)$ and $\varphi_n(y)$ is improved using the shift-and-invert technique as suggested above, the multiplication by $\sin(k_n y)$ and $\sin(k_n x)$ respectively should be treated with care. Indeed, if γ is chosen too large, the exponential growth of these sine functions may still introduce a blow-up of round-off errors in the computation. To avoid this issue, the rotation angle γ should always be chosen as small as possible, under the condition that the multigrid scheme remains stable. This trade-off in the choice of the complex rotation is characteristic for complex shifted/rotated problems, cf. [14, 11].

5.2. Validation of the complex contour approach: computation of the ionization cross sections

Following the discussion in the previous section, the cross section $\zeta(k_1, k_2)$ of the 2D Temkin-Poet model problem can now be calculated accurately. The TP model problem features potentials $V_1(x) = -1/x$, $V_2(y) = -1/y$ and $V_{12}(x,y) = 1/\max(x,y)$, and the right-hand side is given by $f(x,y) = xy\exp(-(x+y)^2)$. The double ionization cross section is given by expression (20), where $k_1 = \sqrt{2E}\sin(\alpha)$ and $k_2 = \sqrt{2E}\cos(\alpha)$. Hence, the cross section $\zeta(k_1, k_2)$ can be calculated for a single energy E in function of the incoming wave angle $\alpha \in [0, \pi/2]$ to yield the single differential cross section (SDCS). The total cross section (TCS) $\sigma_{tot}(E)$ can then be calculated as an integral of ζ over all energy fractions and is given by expression (21) in function of the energy of the system.

Figure 8 (left panel) shows the single differential cross section for the 2D Temkin-Poet model problem for the energy $E = 1$, at which a full break-up of the system (double ionization) occurs. The scattering solution is computed using a spectral element discretization of the domain $\Omega = [0, 108]^2$ using $n_x = n_y = 269$ grid

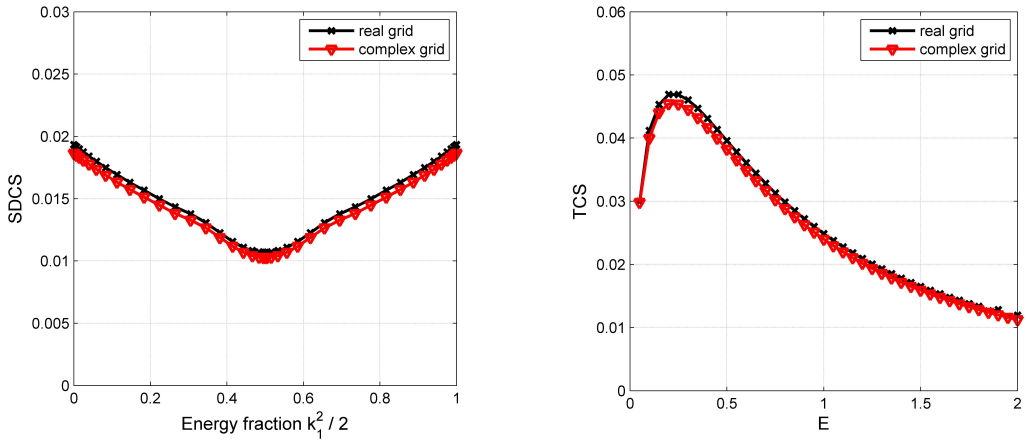

Figure 8: Left: Single differential cross section $\zeta(k_1, k_2)$ (20) in function of the energy fraction $k_1^2/2 \in [0, 1]$. Right: Total double ionization cross section $\sigma_{tot}(E)$ (21) in function of the energy $E \in [0, 2]$. Black: classical calculation on the real-valued domain using ECS boundaries with $\theta_{ECS} = 30°$. Red: alternative calculation on the complex-valued domain with $\gamma = 9°$.

points in every spatial direction. The SDCS is computed on both the complex contour domain with $\gamma = 9°$ and the classical real-valued domain with an ECS absorbing boundary layer ($\theta_{ECS} = 30°$) for comparison. Note that to avoid propagation of numerical eigenstate round-off errors throughout the algorithm, the shift-and-invert technique is applied to the 1D eigenmodes to ensure numerical accuracy. The complex contour approach yields an accurate representation of the SDCS compared to the classical real-valued computation.

The total cross section for the 2D Temkin-Poet model problem is shown in Figure 8 (right panel) for a range of energies $E \in [0, 2]$ for which both single and double ionization occur simultaneously. The figure validates the complex contour approach by comparing the TCS computed using the classical real-valued domain to the computation of the cross section using the complex contour approach, where notably 2 steps of shift-and-invert are included for numerical accuracy. The resulting total cross section is close to identical for both methods.

6. Numerical results: convergence of the MG-CCCS method

In this section we validate the efficiency and scalability of the Multigrid-Coupled Channel (MG-CCCS) combined method for solving the damped Schrödinger equation along a complex contour. We illustrate the convergence of MG-CCCS both as a solver and a Krylov preconditioner. When used as a Krylov preconditioner, only one MG-CCCS V-cycle is used to approximately solve the preconditioning system, as is common practice in the multigrid literature [14, 5].

6.1. The 2D ionization model with exponential potentials

As a proof of concept, we first consider a simple 2D electron-impact ionization model problem with exponentially decreasing potentials. The potentials are given by $V_1(x) = -4.5\exp(-x^2)$, $V_2(y) = -4.5\exp(-y^2)$ and $V_{12}(x, y) = 2\exp(-0.1(x + y)^2)$. The right-hand side is $f(x, y) = \exp(-3(x + y)^2)$. The corresponding driven Schrödinger equation (7) is solved along a complex contour with rotation angle $\gamma = \pi/18 = 10°$ on a uniform discretization of the domain $\Omega = [0, 20]^2$ featuring $n_x = n_y = 256$ grid points in every spatial direction. This ensures a minimum of 20 grid points per wavelength for all energies $E \in [-2, 3]$, yielding an accurate representation of the waveforms.

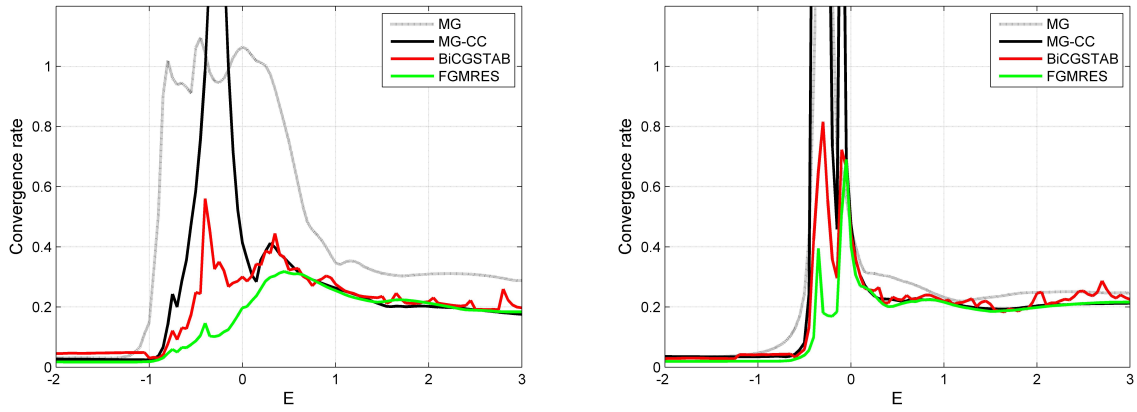

Figure 9: Comparison of the convergence rates of different iterative solution methods for two 2D complex contour Schrödinger model problems. Classical MG is used as a solver only. The MG-CCCS method (with $M = L = 2$) is used both as a stand-alone solver and Krylov preconditioner for BiCGSTAB and FGMRES. Left: exponential potentials model problem, domain $[0, 20]^2$, no. grid points $n_x = n_y = 256$, no. MG levels $l = 8$. Right: Temkin-Poet model problem, domain $[0, 100]^2$, no. grid points $n_x = n_y = 1024$, no. MG levels $l = 10$.

Figure 9 (left panel) compares the convergence rate of the classical multigrid method to the MG-CCCS, MG-CCCS BiCGSTAB and FGMRES solvers in function of the energy. The MG scheme denotes the standard multigrid method using V(1,1)-cycles with a GMRES(3) pre- and post-smoothing substitute. The MG-CCCS scheme includes a Coupled Channel correction step with $L = M = 2$ after each V-cycle. The classical MG solver is instable in the region of energies for which only single ionization occurs, i.e. for $E \in [-1, 0]$, cf. conclusions drawn in [10]. In principle the energy regimes for which only single ionization occurs do not require a full 2D description, since a 1D model would suffice to describe the single ionization waveforms. However, rather than adapting the mathematical model description to the energy E, we in this work aim at constructing a robust 2D solver that is effective for *all* energy regimes.

The MG-CCCS solver features improved convergence for most energy levels due to the additional elimination of 1D evanescent modes from the error. This implies the overall convergence of the MG-CCCS scheme is significantly better than the standard MG convergence rate. Stability of the MG-CCCS scheme is unfortunately still not guaranteed for every energy. However, the MG-CCCS scheme can be used as a preconditioner to a general Krylov method to further improve robustness. Acceleration of the MG-CCCS scheme by a governing Krylov solver leads to a working solution method over the entire energy range. The MG-CCCS preconditioned BiCGSTAB solver features a convergence rate of less than 0.6 for all energy regimes, while the restarted FGMRES(5) features a convergence rate of at most 0.32 for all energies. The MG-CCCS Krylov solver hence proves to be a robust solution method for the 2D ionization model problem.

6.2. The 2D Temkin-Poet model

We now consider a more realistic Temkin-Poet benchmark problem on a large domain $\Omega = [0, 100]$, requiring a fine discretization of $n_x = n_y = 1024$ grid points to satisfy the wavenumber criterion of 20 points per wavelength for all energies $E \in [-2, 3]$. The Temkin-Poet potentials are $V_1(x) = -1/x$, $V_2(y) = -1/y$ and $V_{12}(x, y) = 1/\max(x, y)$, and the right-hand side for this problem is again $f(x, y) = \exp(-3(x + y)^2)$.

The convergence rates for the 2D Temkin-Poet model are shown in the right panel of Figure 9. Note how the effect of the Coupled Channel correction is somewhat less pronounced for the TP model problem. Indeed, a smaller improvement in convergence rate is measured when comparing the classical MG and MG-CCCS schemes. However, the MG-CCCS preconditioned Krylov solvers again provide a stable solution method

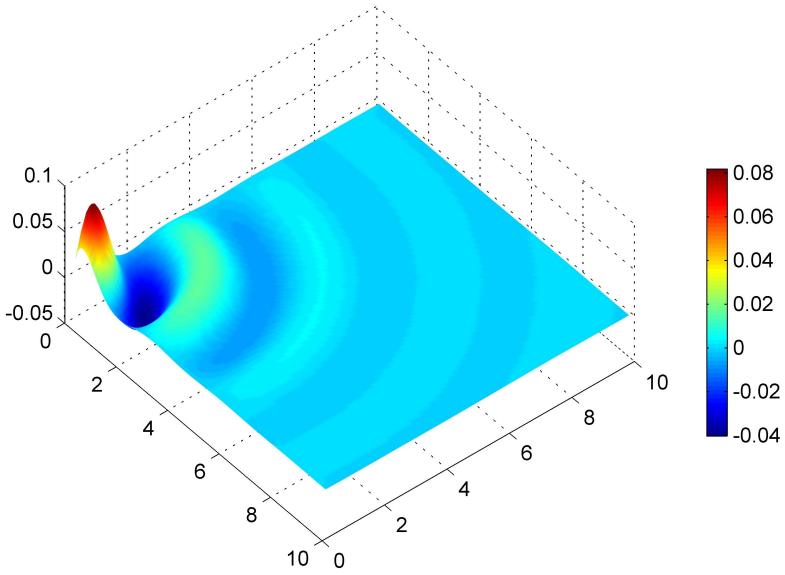

Figure 10: Numerical solution u^N to the 2D complex-valued Temkin-Poet model problem with energy $E = 1$. Discretization of the domain $\Omega = [0, 200]^2$ using a total of 2048^2 grid points. Displayed is a close-up of the solution on the subdomain $[0, 10]^2$. The exponential decay of the solution on the complex rotated grid is clearly visible. Solution method details: see Table 1.

	domain Ω	$[0,10]^2$	$[0,20]^2$	$[0,50]^2$	$[0,100]^2$	$[0,200]^2$
	$n_x \times n_y$	128^2	256^2	512^2	1024^2	2048^2
$E = -2$	iterations	3	3	3	3	3
	total CPU time	0.3 s.	0.9 s.	3.8 s.	15.1 s.	59.4 s.
	time/gridpoint	18.3 μs.	13.7 μs.	14.5 μs.	14.4 μs.	14.2 μs.
$E = -1$	iterations	3	3	3	3	3
	total CPU time	0.3 s.	0.9 s.	3.9 s.	15.2 s.	60.3 s.
	time/gridpoint	18.3 μs.	13.7 μs.	14.9 μs.	14.5 μs.	14.4 μs.
$E = 0$	iterations	5	9	10	11	11
	total CPU time	0.5 s.	2.5 s.	13.0 s.	56.2 s.	227.1 s.
	time/gridpoint	30.5 μs.	38.1 μs.	49.6 μs.	53.6 μs.	54.1 μs.
$E = 1$	iterations	6	7	7	7	7
	total CPU time	0.5 s.	2.1 s.	9.0 s.	35.8 s.	145.1 s.
	time/gridpoint	30.5 μs.	32.0 μs.	34.3 μs.	34.1 μs.	34.6 μs.
$E = 2$	iterations	7	7	7	7	7
	total CPU time	0.6 s.	2.0 s.	9.0 s.	35.4 s.	140.4 s.
	time/gridpoint	36.6 μs.	30.5 μs.	34.3 μs.	33.8 μs.	33.5 μs.
$E = 3$	iterations	7	7	8	8	8
	total CPU time	0.6 s.	2.0 s.	10.3 s.	40.1 s.	162.0 s.
	time/gridpoint	36.6 μs.	30.5 μs.	39.3 μs.	38.2 μs.	38.6 μs.

Table 1: Scalability results for the 2D complex-valued Temkin-Poet model problem for energies $E = -2, -1, 0, 1, 2$ and 3. MG-CCCS preconditioned FGMRES ($M = L = 2$) iteration count, total CPU time and average CPU time per gridpoint required to solve the problem up to a relative residual tolerance of 10^{-6} in function of the problem size. Discretizations respecting the 20 points per wavelength criterion.

for all energies. Convergence rates for the MG-CCCS FGMRES solver generally lie below 0.30, with the exception of a small outlier at slightly negative energies where it rises to around 0.70. Convergence of the MG-CCCS Krylov solver is guaranteed for all $E \in [-2, 3]$, yielding a robust solver for all energy regimes.

Table 1 shows the scalability of the MG-CCCS preconditioned FGMRES solver for the Temkin-Poet model problem for different fixed energy levels $E = -2, -1, 0, 1, 2$ and 3. Note that the energies $E = -2, -1, 0$ correspond to single ionization regime, whereas the energies $E = 1, 2, 3$ represent regions of physical interest where single and double ionization simultaneously occur. The number of MG-CCCS FGMRES iterations, the total CPU time, and the average time per grid point[3] required to solve the problem up to a relative residual tolerance of 10^{-6} are displayed in function of the number of grid points (increasingly more accurate discretization). Perfect $\mathcal{O}(N)$ scalability can be observed from the table for all energies, except for $E = 0$, where a small convergence deterioration is observed. The number of Krylov iterations remains constant as the number of discretization points increases, resulting in a CPU time which effectively scales linearly in the number of unknowns. Moreover, good scalability in function of the energy level is observed. Hence, it is concluded that the MG-CCCS preconditioned Krylov method is not only robust to different energies as shown by Figure 9, it additionally exhibits optimal scaling properties in function of the problem size.

7. Conclusions

In this paper we have developed an efficient and robust multigrid-based computational scheme for the calculation of the ionization cross sections of a Schrödinger-type quantum mechanical break-up problem. The proposed method achieves linear scalability in the number of unknowns. It is based on the so-called complex contour approach [10], i.e. a reformulation of the classical real-valued far field integral (cross section) to an integral over a complex rotated domain. The numerical solution to the underlying driven Schrödinger system (scattered wave) on the complex-valued domain is much easier to obtain iteratively, which overcomes the primary computational bottleneck for the calculation of the ionization cross sections.

The MG-CCCS method proposed in this work combines the functionality of multigrid on the complex-rotated (damped) Schrödinger problem with a Coupled Channel Correction Scheme [18, 22], which accounts for the existence of single ionization waves in the solution that might deteriorate the multigrid convergence. Potentially accelerated by a Krylov subspace method for improved robustness, the MG-CCCS solver is capable of efficient computation of the complex-valued scattered wave for any energy E, featuring optimal $\mathcal{O}(N)$ scalability in the number of unknowns. Furthermore, the Coupled Channel Correction Scheme improves the stability of the classical multigrid method, ensuring robustness of the MG-CCCS Krylov solver with respect to the energy of the system.

Note that there are other possibly remedies for removing the remaining errors caused by the presence of single ionization waves along the axes. For example, a semi-coarsening strategy that removes grid points in the middle of the domain but keeps sufficient points along the axes might also efficiently remove these errors. Furthermore, note that the Coupled Channel Correction Scheme proposed in this work shows resemblance to a deflation strategy. In this paper the CCCS was implemented as an explicit additional step to increase the performance of the multigrid preconditioner. However, it could alternatively be embedded in the governing Krylov solver in the form of a deflation step, cf. the work by Sheikh et al. [30], which analogously aims at eliminating problematic eigenstates in the solution and may lead to an even more efficient solver.

Particular care is advised when solving impact ionization problems on the complex-valued domain, since the complex integral implementation is prone to round-off errors due to the exponential decay and growth of the eigenstates and incoming wave components respectively. Consequently, numerical round-off errors might

[3] System specifications: Intel Core i7-2720QM 2.20GHz CPU, 6MB Cache, 8GB RAM.

propagate through the algorithm and contaminate the resulting cross sections when not treated properly. We suggested the use of a shift-and-invert technique to ensure proper accuracy of the eigenstate functions for impact ionization simulations.

The choice of the complex rotation angle is of fundamental importance in this regard, since it governs the rate of exponential growth of particular integrand components. Although from the analytical viewpoint there are no fundamental restrictions on the magnitude of the complex rotation, and despite the fact that the multigrid solver clearly benefits from a heavy damping of the problem, we have shown that choosing the rotation angle too large may result in numerical instabilities when calculating the far field integral. Hence, the rotation angle is bounded both from below by the requirement of a stable multigrid solver, and from above by the numerical accuracy of the implementation. A mindful trade-off between these two conditions should be achieved in order to obtain a functional computational scheme.

As shown in this paper, the MG-CCCS method allows for a linear scaling of the computational time in function of the number of unknowns. Sublinear scaling may be achieved by a parallel implementation of the multigrid solver, which will be treated in future work.

Numerical results on the 2D Temkin-Poet benchmark problem validate the proposed MG-CCCS complex contour approach, showing the method to yield an accurate representation of the single differential and total double ionization cross sections for the two-body electron break-up problem. Although the results provided in this paper are restricted to 2D model problems for notational and implementation convenience, the extension of the proposed MG-CCCS method to higher spatial dimensions, notably the three-particle break-up system, is straightforward and will also be treated as part of future work.

Acknowledgments

This research is funded by the Research Council of the University of Antwerp. The authors additionally thank Bram Reps for fruitful discussions on the subject.

References

[1] G.B. Arfken and H.J. Weber. *Mathematical Methods For Physicists*. Academic press, 1995.

[2] M. Baertschy, T.N. Rescigno, W.A. Isaacs, X. Li, and C.W. McCurdy. Electron-impact ionization of atomic hydrogen. *Physical Review A*, 63(2):022712, 2001.

[3] E. Balslev and J.M. Combes. Spectral properties of many-body Schrödinger operators with dilatation-analytic interactions. *Communications in Mathematical Physics*, 22(4):280–294, 1971.

[4] J.-P. Berenger. A perfectly matched layer for the absorption of electromagnetic waves. *Journal of computational physics*, 114(2):185–200, 1994.

[5] M. Bollhöfer, M.J. Grote, and O. Schenk. Algebraic multilevel preconditioner for the Helmholtz equation in heterogeneous media. *SIAM Journal on Scientific Computing*, 31(5):3781–3805, 2009.

[6] A. Brandt. Multi-level adaptive solutions to boundary-value problems. *Mathematics of computation*, 31(138):333–390, 1977.

[7] W.L. Briggs, V.E. Henson, and S.F. McCormick. *A Multigrid Tutorial*. Society for Industrial Mathematics, Philadelphia, 2000.

[8] H. Calandra, S. Gratton, R. Lago, X. Pinel, and X. Vasseur. Two-level preconditioned Krylov subspace methods for the solution of three-dimensional heterogeneous Helmholtz problems in seismics. Technical report, TR/PA/11/80, CERFACS, Toulouse, France, 2011.3, 2011.

[9] D.L. Colton and R. Kress. *Inverse acoustic and electromagnetic scattering theory*, volume 93. Applied Mathematical Sciences, Springer, 1998.

[10] S. Cools, B. Reps, and W. Vanroose. An efficient multigrid calculation of the far field map for Helmholtz and Schrödinger equations. *SIAM Journal on Scientific Computing*, 36(3):B367–B395, 2014.

[11] S. Cools and W. Vanroose. Local Fourier analysis of the complex shifted Laplacian preconditioner for Helmholtz problems. *Numerical Linear Algebra with Applications*, 20(4):575–597, 2013.

[12] H. Elman, M. Mihajlović, and D. Silvester. Fast iterative solvers for buoyancy driven flow problems. *Journal of Computational Physics*, 230(10):3900–3914, 2011.

[13] H.C. Elman, O.G. Ernst, and D.P. O'Leary. A multigrid method enhanced by Krylov subspace iteration for discrete Helmholtz equations. *SIAM Journal on Scientific Computing*, 23(4):1291–1315, 2002.

[14] Y.A. Erlangga, C.W. Oosterlee, and C. Vuik. A novel multigrid based preconditioner for heterogeneous Helmholtz problems. *SIAM Journal on Scientific Computing*, 27(4):1471–1492, 2006.

[15] O.G. Ernst and M.J. Gander. Why it is difficult to solve Helmholtz problems with classical iterative methods. In *Numerical Analysis of Multiscale Problems. Durham LMS Symposium.* Citeseer, 2010.

[16] H. Friedrich. *Theoretical atomic physics*, volume 3. Springer, 2006.

[17] R.G. Grimes, J.G. Lewis, and H.D. Simon. A shifted block Lanczos algorithm for solving sparse symmetric generalized eigenproblems. *SIAM Journal on Matrix Analysis and Applications*, 15(1):228–272, 1994.

[18] E.J. Heller and W.P. Reinhardt. Comment on the direct-matrix solution of a singular Lippmann-Schwinger equation. *Physical Review A*, 7:365–367, 1973.

[19] S.G. Johnson. Saddle-point integration of C^∞ "bump" functions. *Manuscript. Available at http://math.mit.edu/∼stevenj/bump-saddle.pdf*, 2007.

[20] A. Kirsch. *An introduction to the mathematical theory of inverse problems*, volume 120. Applied Mathematical Sciences, Springer, 1996.

[21] M.M.M. Made. Incomplete factorization-based preconditionings for solving the Helmholtz equation. *Int. J. Numer. Meth. Eng.*, 50(5):1077–1101, 2001.

[22] I.E. McCarthy and A.T. Stelbovics. Momentum-space coupled-channels optical method for electron-atom scattering. *Physical Review A*, 28(5):2693–2707, 1983.

[23] C.W. McCurdy, M. Baertschy, and T.N. Rescigno. Solving the three-body Coulomb breakup problem using exterior complex scaling. *Journal of Physics B: Atomic, Molecular and Optical Physics*, 37(17):R137, 2004.

[24] C.W. McCurdy, T.N. Rescigno, and D. Byrum. Approach to electron-impact ionization that avoids the three-body Coulomb asymptotic form. *Physical Review A*, 56(3):1958, 1997.

[25] K.O. Mead and L.M. Delves. On the convergence rate of generalized Fourier expansions. *IMA Journal of Applied Mathematics*, 12(3):247–259, 1973.

[26] N. Moiseyev. Quantum theory of resonances: calculating energies, widths and cross-sections by complex scaling. *Physics Reports*, 302(5):212–293, 1998.

[27] B. Reps, W. Vanroose, and H. bin Zubair. On the indefinite Helmholtz equation: Complex stretched absorbing boundary layers, iterative analysis, and preconditioning. *Journal of Computational Physics*, 229(22):8384–8405, 2010.

[28] T.N. Rescigno, M. Baertschy, W.A. Isaacs, and C.W. McCurdy. Collisional breakup in a quantum system of three charged particles. *Science*, 286(5449):2474–2479, 1999.

[29] C.D. Riyanti, Y.A. Erlangga, R.E. Plessix, W.A. Mulder, C. Vuik, and C. Oosterlee. A new iterative solver for the time-harmonic wave equation. *Geophysics*, 71(5):E57–E63, 2006.

[30] AH Sheikh, D Lahaye, and C Vuik. On the convergence of shifted laplace preconditioner combined with multilevel deflation. *Numerical Linear Algebra with Applications*, 20(4):645–662, 2013.

[31] B. Simon. The definition of molecular resonance curves by the method of Exterior Complex Scaling. *Physics Letters A*, 71(2):211–214, 1979.

[32] U. Trottenberg, C.W. Oosterlee, and A. Schüller. *Multigrid*. Academic Press, New York, 2001.

[33] H.A. Van der Vorst. *Iterative Krylov methods for large linear systems*, volume 13. Cambridge University Press, 2003.

[34] W. Vanroose, D.A. Horner, F. Martin, T.N. Rescigno, and C.W. McCurdy. Double photoionization of aligned molecular hydrogen. *Physical Review A*, 74(5):052702, 2006.

[35] W. Vanroose, F. Martin, T.N. Rescigno, and C.W. McCurdy. Complete photo-induced breakup of the h_2 molecule as a probe of molecular electron correlation. *Science*, 310(5755):1787–1789, 2005.

[36] J.H. Wilkinson. *Rounding errors in algebraic processes*. Courier Dover Publications, 1994.